Pergamon

Int. J. Heat Mass Transfer. Vol. 37, No. 7, pp. 1081–1094, 1994

0017–9310/94 $6.00 + 0.00

0017–9310(93)E0033–D

Natural convection in porous media with anisotropic dispersive thermal conductivity

L. E. HOWLE

Mechanical Engineering and Materials Science Department, Box 90300 Duke University, Durham, NC 27708-0300, U.S.A.

and

J. G. GEORGIADIS

Mechanical and Industrial Engineering Department, University of Illinois at Urbana-Champaign, Urbana, IL 61801, U.S.A.

(*Received* 28 *April* 1993 *and in final form* 2 *November* 1993)

Abstract—A numerical simulation is undertaken in order to study the effect of anisotropy of the effective thermal conductivity tensor on heat transport in the porous medium Rayleigh–Bénard problem. The momentum equation includes an inertial drag (Forchheimer) term. The effective thermal conductivity tensor, in the energy equation, contains an isotropic stagnant component and a hydrodynamic dispersive component with principal axes aligned with the local velocity vector and with magnitude proportional to the local velocity amplitude. A parametric study of two-dimensional steady cellular convection reveals the following. (1) Dispersion increases the net heat transfer after a Rayleigh number ~ 100–200. As the degree of anisotropy of the effective thermal conductivity is increased, the wall averaged Nusselt number is decreased. (2) Using the available Rayleigh number–wavenumber variation data does not affect the divergence between simulation and experiment.

1. INTRODUCTION

THE STUDY of buoyancy driven convection in fluid-saturated porous media is motivated by applications in such diverse areas of technology as oil and groundwater resource management, control of the spread of underground pollutants, porous insulation, and binary alloy solidification, cf. Georgiadis [1]. Such physical systems can be prohibitively complex since they involve multicomponent convection, chemical reaction, and complicated pore structure. It is desirable to first focus on a uniform system, simple enough to allow analysis with reasonable effort, yet retain enough physics so that valuable insight can be gained. The problem we consider here is single-component natural convection in a layer of infinite horizontal extent, bounded by impermeable upper and lower walls and filled with a fluid-saturated porous medium. When heated from below, a spontaneous initiation of cellular fluid motion is observed. This is essentially the analogue of the classical Rayleigh–Bénard convection (RBC) in pure fluid. Adopting the suggestion of Nield and Bejan [2], we will refer to the problem under consideration as Horton–Rogers–Lapwood convection, HRLC for short.

Despite many thorough theoretical studies, see for example Joseph [3] and Nield and Bejan [2], the HRLC problem is not as well characterized as its counterpart in pure fluid. One particularly persistent problem is the reported uncertainty as to the correct governing equations for buoyancy driven convection in porous media. This is manifested by the fact that there is a large-scale discrepancy between Nusselt number measurements and predictions based on the Darcian model. Employment of nonlinear non-Darcian models in HRLC was first reported in the analytical work of Neischloss and Dagan [4], and the numerical studies of Kvernvold and Tyvand [5], and Georgiadis and Catton [6, 7]. The first two articles employ an anisotropic quadratic dispersion model, the third examines the effect of the Forchheimer (quadratic) drag term, while the forth includes the effect of both the Forchheimer term and an isotropic linear hydrodynamic dispersion term. Kvernvold and Tyvand [5] reported that the effect of the dispersive enhancement of conductivity (which is characterized by the dispersion factor $(d/L)^2(k_m/k_f)$, where d/L expresses the coarseness of the packed bed) is to increase the Nusselt number. Georgiadis and Catton [6] found that the Nusselt number decreases as the parameter $\omega = (bL)/(\gamma Pr)$ increases. Finally, Georgiadis and Catton [7] found that the inclusion of the dispersion term explains certain anomalous heat transfer data reported in the literature. On the basis of the isotropic dispersion model, it was also concluded that, unless the Prandtl number is 0.01 or less, dispersion dominates the quadratic drag and increases the Nusselt number.

NOMENCLATURE

a_m	thermal diffusivity of the medium, $k_m (\rho c)_f^{-1}$ [m^2 s^{-1}]
A_0, A_k	Fourier coefficients of the velocity amplitude, equation (21)
b	inertial resistance coefficient, $1.75d(150(1-\phi))^{-1}$ [m]
B_0, B_k	Fourier coefficients of nonlinear terms involving velocity amplitude, equation (22)
c	specific heat [J kg^{-1} K^{-1}]
C_k	Fourier coefficients of nonlinear terms involving velocity amplitude, equation (24)
C_L	longitudinal dispersion coefficient, equation (6a)
C_T	transverse dispersion coefficient, equation (7a)
d	bead diameter [m]
D_L	ratio of longitudinal dispersive to stagnant porous medium conductivity, equation (6b)
D_T	ratio of transverse dispersive to stagnant porous medium conductivity, equation (7b)
$\mathbf{D}^*$	dispersivity tensor, equation (3)
Da	Darcy number, γL^{-2}
g	gravitational acceleration in the z-direction [m s^{-2}]
k_L^*	longitudinal effective thermal conductivity, equation (6b) [W m^{-1} K^{-1}]
k_m	stagnant thermal conductivity of porous medium [W m^{-1} K^{-1}]
k_T^*	transverse effective thermal conductivity, equation (7b) [W m^{-1} K^{-1}]
K	number of Fourier modes in the y-direction
KC	Kozeny–Carman inertial coefficient, $\gamma(bL)^{-1}$
L	characteristic macroscopic length, thickness of layer [m]
Nu	Nusselt number, equation (5)
P	average pressure of the interstitial fluid
Pr_m	Prandtl number of the medium, ν/a_m
$\mathbf{q}$	Darcy (superficial) velocity, $(v^2+w^2)^{1/2}$
Ra	Rayleigh number, $g\beta\Delta TL^3(\nu_f a_m)$
Ra_m	porous Rayleigh number, $g\beta\Delta TL\gamma(\nu_f a_m)^{-1}$
t	time [s]
ΔT	temperature difference, $T_H - T_C$ [K]
v, w	horizontal, vertical velocity component, respectively
y, z	horizontal, vertical Cartesian coordinate, respectively.

Greek symbols

α	wavenumber, $2\pi\lambda^{-1}$
β	volumetric thermal expansion of the fluid [K^{-1}]
γ	permeability of the porous medium, $d^2\phi^3(150(1-\phi)^2)^{-1}$ [m^2]
Δ	$D_L - D_T$
δ_{ij}	$\delta_{ij} = 1$ if $i = j$, $\delta_{ij} = 0$ if $i \neq j$
λ	wavelength of basic convection rolls
ν	kinematic viscosity [m^2 s^{-1}]
ρ	fluid density [kg m^{-3}]
ϕ	porosity
ω	inertial drag coefficient, $bL(\gamma Pr_m)^{-1}$.

Subscripts

C	cold
f	fluid
H	hot
k	kth order
m	porous medium
L	longitudinal
T	transverse.

Special symbols

D	z-derivative
$O(\ )$	order of magnitude
DF	Darcy–Forchheimer model, $D_L = D_T = 0$
DFI	Darcy–Forchheimer isotropic model, $D_L = D_T$
DFA3	Darcy–Forchheimer anisotropic model, $D_L/D_T = 3$
DFA4	Darcy–Forchheimer anisotropic model, $D_L/D_T = 4$
Ra_m^{crit}	critical value.

The above numerical investigations [5–7] have somewhat decreased the disagreement between predictions and measurements of the Nu vs Ra_m relationship. Agreement (within experimental error) was achieved in certain subsets of available experimental data. For example, Kvernvold and Tyvand [5] compare only with water–glass data, and Georgiadis and Catton [7] confine their study to the slightly supercritical range $60 < Ra_m < 150$. Although an explanation for the large-scale divergence of the Nu vs Ra_m data was offered by Georgiadis and Catton [6], the same article points out another deficiency in our understanding of the HRLC problem: the lack of flow pattern visualization data which denies closure to the wavenumber selection problem. We would like to point out that the theoretical models in refs. [5–7] involve 2-D periodic flow in layers of infinite horizontal extent, while experiments take place in boxes of various shapes and aspect ratios which produce convection with wave patterns influenced by initial

conditions or wall effects. Moreover, the presence of the porous medium does not allow direct flow visualization. Detailed information about convective patterns, which accelerated the understanding of the Rayleigh–Bénard problem, is unavailable in the HRLC problem. In spite of the above deficiencies, numerical studies of various HRLC models in simple domains are extremely useful in helping to establish correct governing equations for natural convection. They can help test different constitutive laws for flow through porous media: the correct law will ultimately eliminate inconsistencies between theory and experiment. A major part of our uncertainty concerning such laws is related to the definition of 'effective' thermophysical properties such as the thermal conductivity. The effective thermal conductivity is traditionally represented by the conductivity of the stagnant fluid-saturated porous medium augmented by a dispersive component which is caused by the motion of the interstitial fluid. Numerical studies have demonstrated that the effect of dispersion on the HRLC problem and its variations is significant when the porous layer is coarse (L/d is of order 10 or less), see also He and Georgiadis [8]. The isotropic conductivity model adopted by Georgiadis and Catton [7] seems to generally overpredict the Nusselt number. We therefore seek to explore an anisotropic version of that model, as suggested by Georgiadis and Catton [6].

In this article, we study the effect of anisotropic dispersion on heat transfer in the presence of inertia (Forchheimer) drag. The Darcy–Forchheimer–Boussinesq formulation of the momentum equation, along with slip boundary conditions, is coupled to a single energy equation which contains the full anisotropic tensor of effective thermal conductivity. While valid theoretical models exist for the longitudinal component of the conductivity tensor, the magnitude of the transverse component is a point of contention. We use ratios of longitudinal to transverse dispersivities of 3.0 and 4.0, since Saffman [9] proposed (and Kvernvold and Tyvand [5] used) a value of 40/15. We also evaluate the dispersivity values proposed by Hsu and Cheng [10].

The layout of this paper is as follows. In Section 2, the system of equations governing porous natural convection with anisotropic dispersive thermal conductivity is presented. The parameters which characterize the system are defined, followed by a discussion of boundary conditions. A brief description of the numerical scheme is also included. A discussion of the numerical results and comparison with available experimental data is given in Section 3. Conclusions are presented in Section 4.

2. THE MATHEMATICAL MODEL

HRLC, as its pure fluid counterpart RBC, is formally defined as natural convection in differentially heated horizontal layers of infinite lateral extent. A number of simplifying assumptions are made in order to make HRLC solvable.

1. The porous media, as exemplified by packed beds sandwitched between impermeable isothermal plates, are assumed to be homogeneous and isotropic. This means that we cannot discriminate between different packings and aspect ratios (ratio of horizontal and vertical dimensions) of reported experiments. Indeed, many researchers fail to report detailed structural data for the packed beds they use.

2. Available theoretical [2, 3, 7] and recent experimental work [11] on HRLC indicate that, under certain conditions (including assumption 1), there is a sharp transition (bifurcation) from the motionless conduction state to a steady two-dimensional convection when a non-dimensional number, Ra_m, attains the critical value $4\pi^2$. This state is stable and consists of pairs of counter-rotating straight rolls with period λ. Without loss of generality, we can then consider the plane normal to the rolls, see Fig. 1. Unless otherwise indicated, we will set $\lambda = 2L$, which corresponds to the critical wavelength at the onset of convection.

2.1. *System of equations*

Because the equations governing heat transport and fluid flow for porous media have been developed in an empirical manner, the equations will not be derived here. We adopt the incompressible Darcy–Forchheimer–Boussinesq formulation of the momentum equation and the dispersive energy equation. This is the same system of equations used by Georgiadis and Catton [7] for their study of isotropic dispersive thermal conductivity. The present work uses an anisotropic dispersivity tensor (discussed in Section 2.4) in the energy equation as proposed by Georgiadis and Catton [6]. The governing equations, in non-dimensional form, are

$$\nabla \cdot \mathbf{q} = 0, \tag{1}$$

$$\frac{1}{\phi Pr_m}\frac{\partial q}{\partial t} = -\nabla P + RaTe_z - \frac{1}{Da}\mathbf{q} - \omega|\mathbf{q}|\mathbf{q}, \tag{2}$$

$$\frac{(\rho c)_m}{(\rho c)_f}\frac{\partial T}{\partial t} = -\mathbf{q}\cdot\nabla T + \nabla\cdot[(1+\mathbf{D}^*)\nabla T]. \tag{3}$$

The scales used in the non-dimensionalization of (1)–(3) are length $\sim L$, velocity $\sim a_m L^{-1}$, pressure $\sim \rho v a_m L^{-2}$, and temperature $\sim \Delta T$.

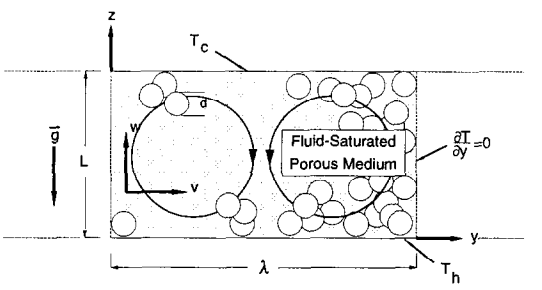

FIG. 1. Isolated convection cell.

2.2. *Boundary conditions*

The temperature in equations (2) and (3) is scaled between zero and one. The temperature boundary condition is unity at the lower horizontal boundary and zero at the upper horizontal boundary of Fig. 1. Symmetry considerations imply that the two lateral boundaries are adiabatic since only straight rolls are considered.

The impenetrability condition employed here requires that the normal component of velocity be zero at the solid walls:

$$\mathbf{q}\cdot\hat{n} = 0 \quad \text{at } z = 0, 1 \tag{4}$$

where n is directed into the porous later. The tangential component of velocity does not vanish at the wall. Although the no slip condition holds on individual pore walls, the spacial averages over many pores (needed to define the Darcy velocity $\mathbf{q}$) produce non-zero velocity at the porous medium–solid wall interface.

2.3. *Thermophysical parameters*

The structure of the porous medium is characterized by the pore size (or bead diameter) d, the layer thickness L, and the local porosity (or void fraction) ϕ. On the basis of assumption (1), we adopt Ergun's [12] empirical formulas for the permeability, γ, and inertial resistance coefficient, b, both defined in the Nomenclature. The thermal properties of the fluid-saturated matrix are expressed by the stagnant thermal conductivity of the medium, k_m (average conductivity when the filtration velocity is zero), and the thermal capacity of the fluid $(\rho c)_f$. We can then define the dimensionless thermophysical parameters of the porous medium ω, Pr_m, and Ra (see Nomenclature). Finally, with the introduction of the Darcy number (which is essentially a coarseness factor) Da, the porous Rayleigh number is defined as $Ra_m = RaDa$. Ra_m is the bifurcation parameter of the system of equations (1)–(3) and accounts for the presence of two length scales: a macroscopic scale, L, the layer thickness, and through a microscopic scale, d, the pore or bead diameter ($\gamma \sim d^2$).

The net dimensionless heat transfer across the cavity, defined as the ratio of the total convective heat flux to its value in the absence of convection, is given by the wall averaged Nusselt number at the bottom wall (or by the spatial average on any horizontal plane),

$$Nu = -\frac{\alpha}{\pi}\int_0^{\pi/\alpha}\left[(1 + D_T|\mathbf{q}|)\frac{\partial T}{\partial z}\right]_{z=0} \mathrm{d}y. \tag{5}$$

Note the presence of the amplitude of the local velocity at the wall. This is a consequence of the velocity dependent enhancement of the effective thermal conductivity owing to dispersion, as described in the following subsection. Because the local velocity is averaged over many pores, there is a slip velocity at the porous medium–solid wall interface, see equation (4).

2.4. *The dispersivity tensor*

Let us consider the two-dimensional flow over an array of cylinders shown in Fig. 2 which is qualitatively similar the flow through packed beds. Fluid particles, traveling along separate paths will be pushed apart, and thus dispersed by the solid obstructions. This is the physical reasoning behind the concept of transverse hydrodynamic dispersion. In a similar manner, longitudinal hydrodynamic dispersion may be thought of as arising due to the fact that the cylinders accelerate fluid packets in adjacent streamlines. The microscopic velocity fields contain regions of slow flow (e.g. boundary layers, cf. Taylor [13]), in which the particles slow down or get trapped, and regions of faster (than the mean) flow which accelerate the particles.

The phenomenon of thermal hydrodynamic dispersion with solid phase participation is more complicated since hydrodynamic dispersion in the fluid is coupled to conduction in the solid. Although the net effect is macroscopically manifested as diffusion (hence the definition of an 'effective' transport coefficient $\mathbf{D}^*$ in equation (3)), the diffusivity can be evaluated only if the microscopic field is known. This is essentially a closure problem. Measurements of the $\mathbf{D}^*$ components are made indirectly by matching with macroscopic transport measurements. An additional complication arises since all measurements of the longitudinal component are made with transient experiments while the transverse component is traditionally obtained at steady-state. Georgiadis and Catton [6] solved a stochastic transport equation based on *a priori* statistics of the interstitial field in porous media to derive the energy equation (3). The anisotropic dispersivity tensor $\mathbf{D}^*$ on the right side of (3) accounts for the enhancement of heat transport due to hydrodynamic dispersion. The longitudinal k_L^* and transverse k_T^* components of $\mathbf{D}^*$ correspond to the directions along and normal to the local (Darcy) velocity, respectively. Georgiadis and Catton [6] derived the expression for the longitudinal transport coefficient

$$k_L^* = k_m\left(1 + \frac{C_L}{1-\phi}\frac{d}{L}|\mathbf{q}|\right). \tag{6a}$$

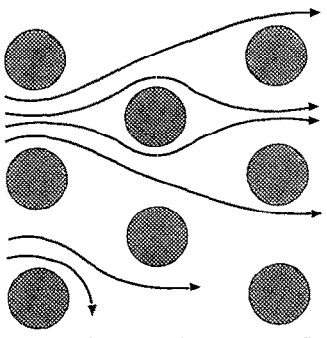

FIG. 2. Hydrodynamic dispersion due to flow through stationary solid matrix.

As mentioned earlier, the ratio d/L is a measure of the coarseness of the packed bed. In an analogous manner, the expression for the transverse transport coefficient is

$$k_T^* = k_m\left(1+\frac{C_T}{1-\phi}\frac{d}{L}|\mathbf{q}|\right). \tag{7a}$$

Georgiadis and Catton [7] found the value of $C_L = 0.36$ to give good agreement with the experiments by Levec and Carbonell [14]. For a medium of layer height L, bead diameter d, and uniform porosity ϕ, equations (6a) and (7a) can be also written

$$k_L^* = k_m(1+D_L|\mathbf{q}|) \tag{6b}$$

and

$$k_T^* = k_m(1+D_T|\mathbf{q}|). \tag{7b}$$

Experiments have shown that D_L is greater than D_T. In the present work, we use the values

$$\frac{C_L}{C_T} = \frac{D_L}{D_T} = 3.0 \text{ and } 4.0 \tag{8}$$

which are close to the ratio 40/15 used by Saffman [9] and Kvernvold and Tyvand [5]. Hsu and Cheng [10] proposed a similar expression for transverse dispersion valid at high Reynolds numbers. When compared to equation (7a), their expression is equivalent to ours if we take $C_T = 0.18/4$ and $C_L = 0.18$ for the Darcy–Forchheimer anisotropic model with $C_L/C_T = 4.0$.

By definition, the local velocity vector is aligned with the principal axis of the $\mathbf{D}^*$ tensor. Referring to the Cartesian system of Fig. 1, where $q_1 = v$ and $q_2 = w$ are the local velocity components, and to equations (6b) and (7b), the components of the conductivity tensor can be expressed as

$$k_{ij}^* = k_m\left(\delta_{ij}+D_T|\mathbf{q}|\delta_{ij}+(D_L-D_T)\frac{q_iq_j}{|\mathbf{q}|}\right) \tag{9}$$

where δ_{ij} is the Kronecker delta.

The two terms D_L and D_T of equations (6b) and (7b), respectively, are the constants of proportionality which account for the enhancement of effective thermal conductivity when flow is present. Further, since $|\mathbf{q}|$ is positive, k_L^* and k_T^* are always greater than or equal to k_m if the velocity is non-zero.

We now return to the Nusselt number given by expression (5). We see that dispersion can increase the net heat transfer, compared to the $D_T = D_L = 0$ case, provided the term $D_T|\mathbf{q}|$ makes a comparatively small change in the temperature gradient at the bottom wall. This is indeed the case and this point will be discussed in more detail in Section 3.2. Since the impenetrable, stress free-boundary condition only allows parallel flow at the wall, D_L does not enter the expression for Nu.

2.5. *Steady state convection: method of solution*

By letting $\mathbf{q} = ve_y + we_z$, considering the steady state, and using (9), the system of governing equations (1)–(3) becomes

$$\frac{\partial v}{\partial y}+\frac{\partial w}{\partial z} = 0, \tag{10}$$

$$\frac{\partial P}{\partial y}+\frac{1}{Da}v+\omega|\mathbf{q}|v = 0, \tag{11}$$

$$\frac{\partial P}{\partial z}-Ra\,T+\frac{1}{Da}w+\omega|\mathbf{q}|w = 0, \tag{12}$$

$$\frac{\partial}{\partial z}\left[\left(1+D_T|\mathbf{q}|+\Delta\frac{w^2}{|\mathbf{q}|}\right)\frac{\partial T}{\partial z}\right]+\frac{\partial}{\partial z}\left[\Delta\frac{wv}{|\mathbf{q}|}\frac{\partial T}{\partial y}\right]+\frac{\partial}{\partial y}\left[\left(1+D_T|\mathbf{q}|+\Delta\frac{v^2}{|\mathbf{q}|}\right)\frac{\partial T}{\partial y}\right]+\frac{\partial}{\partial y}\left[\Delta\frac{wv}{|\mathbf{q}|}\frac{\partial T}{\partial z}\right] = v\frac{\partial T}{\partial y}+w\frac{\partial T}{\partial z} \tag{13}$$

where $\Delta \equiv D_L - D_T$.

We seek a velocity field which satisfies the solenoidal condition, equation (10), and has zero normal velocity at the horizontal boundaries. Additionally, a temperature field is needed which satisfies the temperature boundary condition discussed in Section 2.2. Referring to Fig. 1, the velocity, temperature, and pressure are assumed to be spatially periodic in y with period λ. Since we are considering straight rolls, the solution (v,w,P,T) is projected onto a finite dimensional Fourier space (dimension $K+1$) as follows:

$$v(y,z) \simeq \sqrt{(2)}\sum_{k=1}^{K} v_k(z)\sin(\alpha_k y), \tag{14}$$

$$w(y,z) \simeq \sqrt{(2)}\sum_{k=1}^{K} w_k(z)\cos(\alpha_k y), \tag{15}$$

$$T(y,z) \simeq T_0(z)+\sqrt{(2)}\sum_{k=1}^{K} T_k(z)\cos(\alpha_k y), \tag{16}$$

$$P(y,z) \simeq P_0(z)+\sqrt{(2)}\sum_{k=1}^{K} P_k(z)\cos(\alpha_k y), \tag{17}$$

where we use the discrete wavenumber spectrum $\{\alpha_k\} = k\cdot\alpha$ for $k = 1,2,3\ldots K$.

The boundary conditions are defined in terms of equations (14)–(16) as

$$\begin{aligned} w_k(0) &= w_k(1) = 0,\\ T_0(0) &= 1, \quad T_0(1) = 0,\\ T_k(0) &= T_k(1) = 0. \end{aligned} \tag{18}$$

The spectral space in y is spanned by the following orthogonal basis functions:

$$\begin{Bmatrix} b_s\\ b_e\\ b_o \end{Bmatrix} = \sqrt{2}\begin{Bmatrix} \dfrac{1}{\sqrt{2}}\\ \cos(\alpha_k y)\\ \sin(\alpha_k y) \end{Bmatrix} \tag{19}$$

and the weighted inner product is defined as follows:

$$\langle f,b\rangle = \frac{\alpha}{\pi}\int_0^{\pi/\alpha} \langle fb\rangle \,\mathrm{d}y. \tag{20}$$

Owing to the existence of nonlinear terms in the left hand side of the governing equations (11)–(13), a pseudo-spectral scheme is presumed to be the most efficient numerical approach. Following Georgiadis and Catton [7], the terms containing $|\mathbf{q}|$ are represented by appropriate Fourier series expansions as follows:

$$|\mathbf{q}| = \sqrt{(v^2+w^2)} \simeq \sqrt{(2)}A_0(z) + \sqrt{(2)}\sum_{k=1}^{K} A_k(z)\cos(\alpha_k y), \tag{21}$$

$$\frac{w^2}{|\mathbf{q}|} \simeq \sqrt{(2)}B_0(z)+\sqrt{(2)}\sum_{k=1}^{K} B_k(z)\cos(\alpha_k y), \tag{22}$$

$$\frac{v^2}{|\mathbf{q}|} \simeq \sqrt{(2)}[A_0(z)-B_0(z)] + \sqrt{(2)}\sum_{k=1}^{K}[A_k(z)-B_k(z)]\cos(\alpha_k y), \tag{23}$$

$$\frac{vw}{|\mathbf{q}|} \simeq \sqrt{(2)}\sum_{k=1}^{K} C_k(z)\sin(\alpha_k y). \tag{24}$$

These expansions preserve the spatial symmetries of the Fourier expansions (14)–(17).

2.6. *Weak formulation of the Galerkin ODEs*

We begin by substituting the expansions (14)–(17) and (21)–(24) into the system (10)–(13). Next we form the inner product (20) between the orthogonal basis (19) and equations (10)–(13). Equation (10) yields $v_k = \mathrm{d}w_k/\mathrm{d}z$ which helps eliminate v_k throughout the system. The pressure gradient is also eliminated by cross-differentiating equations (11) and (12), cf. ref. [7]. We then obtain the so-called weak form of the governing equations:

$$\begin{aligned}&(1+\sqrt{(2)}D_{\mathrm{T}}A_0+\sqrt{(2)}\Delta B_0)\mathrm{D}^2T_0 \\ &\quad+\sqrt{(2)}(D_{\mathrm{T}}\mathrm{D}A_0+\Delta\mathrm{D}B_0)DT_0 \\ &= \sum_{k=1}^{K}\{\mathrm{D}(w_k T_k)-\mathrm{D}(D_{\mathrm{T}}A_k DT_k+\Delta B_k DT_k) \\ &\quad+\mathrm{D}(\Delta\alpha_k C_k T_k)\}\end{aligned} \tag{25}$$

and

$$\begin{aligned}&\left\{1+\sqrt{(2)}(D_{\mathrm{T}}A_0+\Delta B_0)+\frac{1}{\sqrt{2}}(D_{\mathrm{T}}A_{2k}+\Delta B_{2k})\right\}\mathrm{D}^2T_k+\left\{\sqrt{2}(D_{\mathrm{T}}\mathrm{D}A_0+\Delta\mathrm{D}B_0)\right. \\ &\left.+\frac{1}{\sqrt{2}}(D_{\mathrm{T}}\mathrm{D}A_{2k}+\Delta\mathrm{D}B_{2k}+\alpha_{2k}\Delta C_{2k}-W_{2k})\right\}\mathrm{D}T_k \\ &-\{(1+\sqrt{2}D_{\mathrm{T}}A_0+\Delta A_0-\Delta B_0)\alpha_k^2 \\ &+\frac{1}{\sqrt{2}}\left(\alpha_{2k}\alpha_k(D_{\mathrm{T}}A_{2k}+\Delta A_{2k}-\Delta B_{2k})\right. \\ &\left.-\alpha_k\Delta\mathrm{D}C_{2k}-\frac{\mathrm{D}W_{2k}}{2}\right)\Bigg\}T_k = f_3^k\end{aligned} \tag{26}$$

with

$$\frac{1}{Da}(\mathrm{D}^2-\alpha_k^2)w_k+\alpha_k^2 RaT_k = \omega(\alpha_k\mathrm{D}f_1^k+\alpha_k^2 f_2^k) \tag{27}$$

for $k = 1,2,\ldots,K$. In equations (25)–(27), the notation D( ) denotes the z-derivative d( )/dz.

The functionals f_1^k, f_2^k, and f_3^k in (26) and (27) are the projections of the nonlinear terms of (21)–(24) onto mode k:

$$f_1^k = -\frac{\sqrt{2}}{\alpha_k}A_0\mathrm{D}w_k-\frac{1}{\sqrt{2}}\sum_{m=1}^{K}\sum_{n=1}^{K}\frac{1}{\alpha_n}\mathrm{D}w_{k_a}A_m I_1(k,n,m), \tag{28}$$

$$f_2^k = \sqrt{(2)}A_0 w_k+\frac{1}{\sqrt{2}}\sum_{m=1}^{K}\sum_{n=1}^{K} w_n A_m I_2(k,n,m), \tag{29}$$

$$\begin{aligned}f_3^k &= \{w_k-(D_{\mathrm{T}}\mathrm{D}A_k+\Delta\mathrm{D}B_k+\Delta\alpha_k C_k)\}\mathrm{D}T_0 \\ &\quad-(D_{\mathrm{T}}A_k+\Delta B_k)\mathrm{D}^2T_0 \\ &\quad+\frac{1}{\sqrt{2}}\sum_{m=1}^{K}\sum_{n=1}^{K}\left\{\left[-(D_{\mathrm{T}}A_n+\Delta A_n-\Delta B_n)\alpha_n\right.\right. \\ &\quad\left.\left.+\Delta\mathrm{D}C_n+\frac{\mathrm{D}w_n}{\alpha_n}\right]\alpha_m T_m+2\Delta C_n\alpha_m\mathrm{D}T_m\right\}I_1(m,n,k) \\ &\quad+\frac{1}{\sqrt{2}}\sum_{m=1}^{K}\sum_{n=1}^{K}\{(D_{\mathrm{T}}A_n+\Delta A_n-\Delta B_n)\alpha_m^2 T_m \\ &\quad-(\mathrm{D}_T A_n+\Delta B_n)\mathrm{D}^2T_m+[w_n-(D_{\mathrm{T}}\mathrm{D}A_n+\Delta\mathrm{D}B_n \\ &\quad+\Delta C_n\alpha_n)]\mathrm{D}T_m\}I_2(k,n,m)\end{aligned} \tag{30}$$

where $m,n\neq k$. The terms $I_1(k,n,m)$ and $I_2(k,n,m)$ in (28)–(30) represent the definite integrals

$$I_1(k,n,m) = \frac{4\alpha}{\pi}\int_0^{\pi/\alpha}\sin(\alpha_k y)\sin(\alpha_n y)\cos(\alpha_m y)\,\mathrm{d}y = \begin{cases}1, & m=|k-n| \\ -1, & m=k+n \\ 0, & \text{otherwise}\end{cases} \tag{31}$$

and

$$I_2(k,n,m) = \frac{4\alpha}{\pi}\int_0^{\pi/\alpha}\cos(\alpha_k y)\cos(\alpha_n y)\cos(\alpha_m y)\,\mathrm{d}y = \begin{cases}1, & m=|k-n| \text{ or } m=k+n \\ 0, & \text{otherwise.}\end{cases} \tag{32}$$

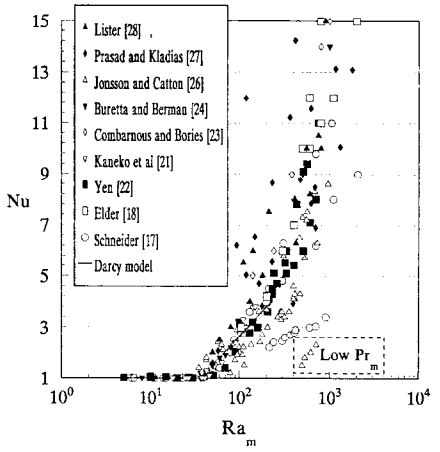

FIG. 3. Experimental heat transfer in fluid-saturated porous media.

2.7. *Linearization*

The system of $2K+1$ ordinary differential equations (25)–(27) (with coefficients defined by (28)—(30)) is linearized and diagonalized with respect to the modal unknowns T_o, T_k, and w_k ($k = 1, 2, \ldots K$) and their derivatives. This is accomplished by moving the terms containing T_k in the right hand side of (30) to the left hand side of (26) and by moving the terms containing w_k in (27) (by virtue of (28), (29)) to the left hand side of (27). The z-derivatives, which consist of terms D^2T_o and DT_o on the left hand side of (25), D^2T_k and DT_k on the left hand side of (26), and D^2w_k in the left hand side of (27), are approximated by second order, centered finite differences on a grid of N uniformly spaced nodes. With this procedure, the $2K+1$ ordinary differential equations are totally modally decomposed and an iterative scheme analogous to the block Gauss–Siedel method is obtained. For each mode k, a tridiagonal system of equations is solved and the new values used to update the next mode $k+1$. After each iteration, the nonlinear terms containing $|\mathbf{q}|$ are updated by transforming them from the physical space to the spectral space by discrete Fourier transformation. The iterations are terminated when the pointwise error criterion

$$\max_{1 \leqslant k \leqslant K} \max_{0 \leqslant z \leqslant 1} \{|w_k^i - w_k^{i-1}|, |T_k^i - T_k^{i-1}|\} < \varepsilon \qquad (33)$$

is satisfied. In equation (33), (i) denotes the modal

Table 1. Input data and experimental references for the cases analyzed

Case	Thermophysical parameters	Numerical parameters	Experimental reference
1 Water–glass $L/d = 27.9$	$Ra_m = 50$–425 $Da = 1.16 \times 10^{-6}$ $Pr_m = 4.00$ $KC = 1.73 \times 10^{-3}$ $\phi = 0.375$	$\varepsilon = 10^{-6}$ $N = 100$ $K = 6$	Prasad and Kladias [27]
2 Water–glass $L/d - 7$	$Ra_m = 50$–400 $Da = 2.08 \times 10^{-5}$ $Pr_m = 4.50$ $KC = 8.70 \times 10^{-3}$ $\phi = 0.394$	$\varepsilon = 10^{-6}$ $N = 100$ $K = 6$	Jonsson and Catton [26]
3 Water–steel $L/d = 8.13$	$Ra_m = 50$–400 $Da = 1.56 \times 10^{-5}$ $Pr_m = 0.92$ $KC = 7.50 \times 10^{-3}$ $\phi = 0.393$	$\varepsilon = 10^{-6}$ $N = 100$ $K = 6$	Jonsson and Catton [26]
4 Water–steel $L/d = 13.1$	$Ra_m = 50$–400 $Da = 6.04 \times 10^{-6}$ $Pr_m = 0.73$ $KC = 4.16 \times 10^{-3}$ $\phi = 0.388$	$\varepsilon = 10^{-6}$ $N = 100$ $K = 6$	Prasad and Kladias [27]
5 100 cs oil–glass $L/d = 20.8$	$Ra_m = 60$–400 $Da = 2.03 \times 10^{-6}$ $Pr_m = 15.7$ $KC = 2.93 \times 10^{-3}$ $\phi = 0.395$	$\varepsilon = 10^{-6}$ $N = 100$ $K = 6$	Jonsson and Catton [26]
6 Mercury–lead $L/d = 26.3$	$Ra_m = 50$–712 $Da = 1.49 \times 10^{-6}$ $Pr_m = 0.018$ $KC = 2.32 \times 10^{-3}$ $\phi = 0.395$	$\varepsilon = 10^{-6}$ $N = 100$ $K = 6$	Jonsson and Catton [26]

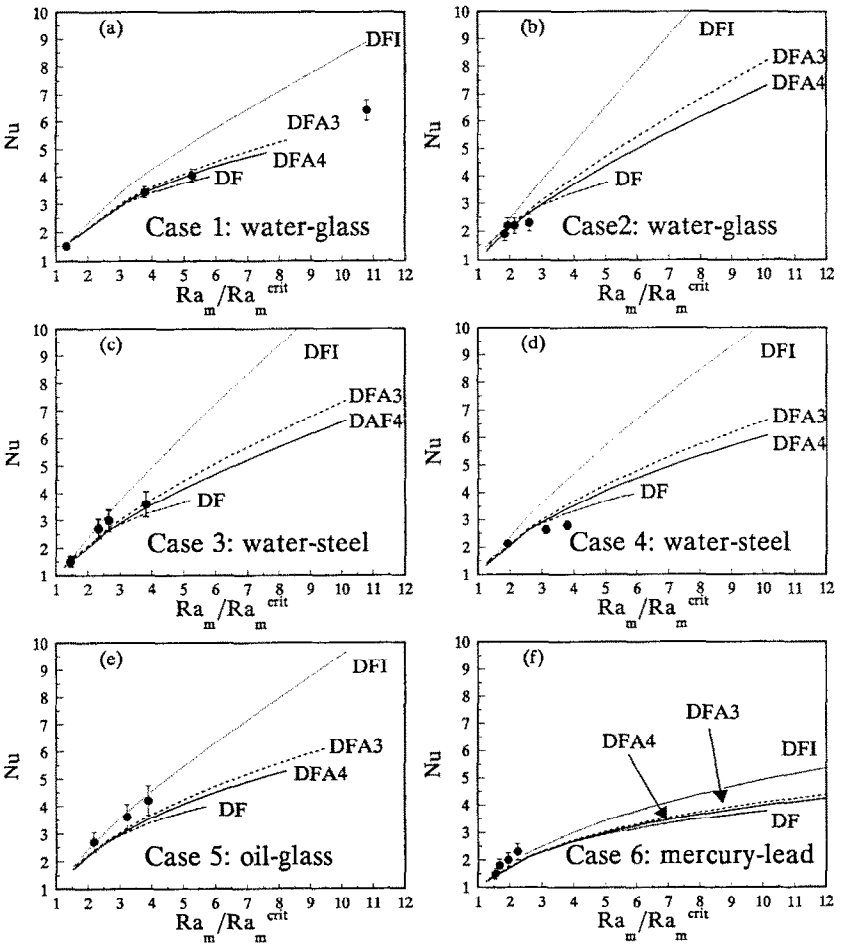

FIG. 4. Comparison between experimental and numerical heat transfer. All cases assume $\alpha = \pi$ with the following notation: DFA4(3), Darcy–Forchheimer anisotropic model ($D_L/D_T = 4(3)$). DFI, Darcy–Forchheimer isotropic model ($D_L = D_T$). DF, Darcy–Forchheimer isotropic model ($D_L = D_T = 0$). (a) Case 1, water–glass, experimental $Ra_m^{crit} = 44$. (b) Case 2, water–glass, experimental $Ra_m^{crit} = 52$. (c) Case 3, water–steel, experimental $Ra_m^{crit} = 77$. (d) Case 4, water–steel, experimental $Ra_m^{crit} = 75$. (e) Case 5, oil–glass, experimental $Ra_m^{crit} = 51$. (f) Case 6, mercury–lead, experimental $Ra_m^{crit} = 319$.

unknown at the i_{th} iteration and ε is the prescribed error tolerance. A fast pseudospectral scheme is obtained. The mean computation time for each value of Ra_m is approximately three minutes on the SGI Personal Iris workstation (model 4D25) with the 25 MHz MIPS R3000A CPU processor (double precision, $K = 6$ Fourier modes, $N = 100$ z-nodes, $\varepsilon = 10^{-6}$).

3. NUMERICAL RESULTS AND DISCUSSION

In order to demonstrate that the numerical method converges, three separate tests are preformed. Convergence tests of the grid function on the z-grid, Newton–Kantorovich iterations and the truncated Fourier series all give satisfactory results, cf. Howle [15]

Experimental studies involving fluid-saturated

Table 2. Numerical values of heat transfer for case 1. $\alpha = \pi$

	Wall averaged Nusselt number, Nu				
Ra_m	Aniso. $D_L/D_T = 4$	Aniso. $D_L/D_T = 3$	Iso. $D_L = D_T$	Forch. $D_L = D_T = 0$	Exper.
58	1.67	1.68	1.74	1.72	1.5
125	3.07	3.13	3.57	3.02	—
164	3.61	3.70	4.40	3.47	3.4
229	4.31	4.47	5.63	4.00	4.0
300	4.88	5.13	6.87	—	—
350	—	—	7.69	—	—

porous media are sparse compared with those of pure fluid. Investigations in porous natural convection were performed by Wooding [16], Schneider [17], Elder [18], Katto and Masuoka [19], Combarnous [20], Kaneko *et al.* [21], Yen [22], Combarnous and Bories [23], and Buretta and Berman [24]. More recent works are by Prasad *et al.* [25], Jonsson and Catton [26], Prasad and Kladias [27], and Lister [28]. As seen in Fig. 3 there exists a large amount of scatter in the data. The four triangular data points, labeled 'low Pr_m', in the figure represent an experiment by Jonsson and Catton [26] involving mercury-saturated beds of lead spheres.

We use the experimental works of Jonsson and Catton [26] and Prasad and Kladias [27] for comparison of prediction with experiment. In Table 1, the thermophysical parameters of the experiments are shown alongside the numerical parameters used for numerical simulation.

3.1. *Heat transfer*

We choose, for definiteness, four different fluid–solid combinations. In addition to the ubiquitous water–glass system data, the intent is to also include data from fluid–solid combinations which do not give good agreement with simulation so that the limitations of the various heat transfer models may be explored. In total, six different fluid–solid matrix systems are examined.

We include natural convection data for the water–glass system from two independent experimental investigations. Figures 4(a) and (b) show the experimental data of Prasad and Kladias [27] and Jonsson and Catton [26], respectively, along with the results of the present simulation (continuous curves). These data are intentionally chosen with widely different L/d (layer height to particle diameter) ratios. Case 1 has a L/d ratio of 27.9 while case 2 has a L/d ratio of 7. We note that the simulation of case 2, which has the fewest bead layers of all cases considered, exhibits higher Nu numbers for all models. The error bound in the Nu measurements is the respective authors' estimate, namely 6% for Prasad and Kladias and 13% for Jonsson and Catton. Refer to the Nomenclature for the notation. All of the simulations shown in Fig. 4 are preformed with the value $C_L = 0.36$, cf. Georgiadis and Catton [7].

In this figure, the Nu data have been plotted against the re-normalized variable Ra_m/Ra_m^{crit}. While we take $Ra_m^{crit} = 4\pi^2$ for the numerical simulations, it varies in the experimental results between cases 1–6 (corresponding to Fig. 4(a)–(f)), as a result of system imperfections and uncertainty in the thermophysical properties. To derive the experimental 'critical' Rayleigh numbers, Ra_m^{crit}, from the experimental data, we use the expression developed by Lage *et al.* [29]:

$$\frac{\dfrac{Nu-1}{Ra}}{\dfrac{}{Ra_m^{crit}}-1} = [C_1(Pr^2)^{-m} + C_2^{-m}]^{-1/m} \qquad (34)$$

for the critical Rayleigh number, Ra_m^{crit}, at the onset of porous natural convection. Lage *et al.* [29] define C_1 and C_2 as

$$C_1 = 172\,Da^{-0.516} \qquad (35)$$

and

$$C_2 = 0.295\,Da^{-0.121}. \qquad (36)$$

Additionally they give the values of m;

$$m = 0.39 \quad \text{for } Da = 10^{-2},$$
$$m = 0.40 \quad \text{for } Da = 10^{-4},$$
$$m = 0.41 \quad \text{for } Da = 10^{-6}. \qquad (37)$$

The critical porous Rayleigh numbers of the experimental data shown in Fig. 4, as computed by equation (34), are listed in the Figure caption. Although these critical values differ, we observe that the agreement between simulation and experiment has been greatly improved when the Ra_m is scaled with an appropriate critical value (obtained from extrapolation). In order to amplify this point, we also compile the same results in direct Nu–Ra_m form in Tables 2–7. A comparison between experiment and theory reveals large differences even close to the onset. Of course, one source of errors comes from property uncertainty. The other is generated by spatial wavenumber uncertainty. Although our numerical simulations generally agree with the predictions of linear stability analysis (this will become apparent shortly), the experimental conditions define a problem slightly different than the canonical HRLC problem (i.e. infinite horizontal layer). All experiments have been preformed in boxes of finite aspect ratio, which essentially limits the range of wavepatterns to those which conform to the box geometry. Following linear stability analysis it can be shown that the variation of the wavenumber away from the theoretical critical for HRLC ($\alpha = \pi$) has a second order effect on Nu when the reduced Ra_m/Ra_m^{crit} is used. This result, in conjunction with the divergence of the Nu–Ra_m results of Tables 2–7, motivated the re-scaling of Ra_m.

We now return to the comparison between the different models. At slightly supercritical Ra_m numbers, the DF model gives the highest Nu. Then at some medium Ra_m (in the range 100–150) the DF and DFA curves cross. This was observed by Kvernvold and Tyvand [5] and Georgiadis and Catton [7]. The predictions according to all models except the DFI model are within the error bounds in Fig. 4(a) (high L/d) while these models overpredict the experiments in Fig. 4(b) (low L/d) for Ra_m/Ra_m^{crit} greater than 2.5.

The next system to be studied is water-saturated bed of steel spheres. This is a system in which the agreement between theory and experiment is poor, for both cases in Tables 4 and 5. All models overpredict the Nusselt number, although it should be noted that this deviation is smaller in the case corresponding to the Jonsson and Catton [26] data. We attribute this to the fact that Jonsson and Catton used measured

Table 3. Numerical values of heat transfer for case 2. $\alpha = \pi$

	Wall averaged Nusselt number, Nu				
Ra_m	Aniso. $D_L/D_T = 4$	Aniso. $D_L/D_T = 3$	Iso. $D_L = D_T$	Forch. $D_L = D_T = 0$	Exper.
50	1.29	1.30	1.35	1.45	—
95	2.47	2.55	3.02	2.55	1.9
111	2.81	2.93	3.59	2.81	2.2
135	3.28	3.46	4.42	3.13	2.3
200	4.41	4.75	6.61	3.78	—
300	5.93	6.54	9.86	—	—

Table 4. Numerical values of heat transfer for case 3. $\alpha = \pi$

	Wall averaged Nusselt number, Nu				
Ra_m	Aniso. $D_L/D_T = 4$	Aniso. $D_L/D_T = 3$	Iso. $D_L = D_T$	Forch. $D_L = D_T = 0$	Exper.
50	1.30	1.31	1.35	1.43	—
113	2.81	2.92	3.56	2.79	1.5
180	3.93	4.18	5.63	3.54	2.7
205	4.28	4.59	6.35	3.74	3.0
295	5.46	5.95	8.85	—	3.6
350	6.10	6.71	10.3	—	—

Table 5. Numerical values of heat transfer for case 4. $\alpha = \pi$

	Wall averaged Nusselt number, Nu				
Ra_m	Aniso. $D_L/D_T = 4$	Aniso. $D_L/D_T = 3$	Iso. $D_L = D_T$	Forch. $D_L = D_T = 0$	Exper.
50	1.34	1.35	1.39	1.43	—
100	2.59	2.66	3.09	2.60	—
143	3.32	3.45	4.31	3.18	2.12
232	4.47	4.74	6.55	3.94	2.63
282	5.00	5.35	7.71	—	2.79
350	5.64	6.11	9.20	—	—

Table 6. Numerical values of heat transfer for case 5. $\alpha = \pi$

	Wall averaged Nusselt number, Nu				
Ra_m	Aniso. $D_L/D_T = 4$	Aniso. $D_L/D_T = 3$	Iso. $D_L = D_T$	Forch. $D_L = D_T = 0$	Exper.
60	1.71	1.72	1.81	1.78	—
111	2.86	2.92	3.37	2.82	2.7
164	3.66	3.78	4.69	3.48	3.6
198	4.08	4.25	5.47	3.79	4.2
250	4.64	4.88	6.60	—	—
325	5.25	5.66	8.16	—	—

values of the stagnant conductivity for the packed beds. The estimation of the effective conductivity in this system is not easy, given the high conductivity ratio of steel to water, $O(100)$. In fact, measurements of the effective thermal conductivity of water–steel systems found in the literature vary over a range of 30%, cf. He and Georgiadis [8].

The solid–fluid combination which gives the best agreement between measurement and simulation in the Nu–Ra_m results is oil-saturated glass beads (case 5). Jonsson and Catton [26] reported the data given in Table 5, and shown in Nu–Ra_m/Ra_m^{crit} form in Fig. 4(e). The DF, DFA4, and DFA3 models agree with measurements within the experimental error. The best agreement over the Ra_m range of the experimental data, as also indicated in Table 5, is given with the DFA4 model.

The last set to be analyzed, case 6, involves mercury-

Table 7. Numerical values of heat transfer for case 6. $\alpha = \pi$

	Wall averaged Nusselt number, Nu				
Ra_m	Aniso. $D_L/D_T = 4$	Aniso. $D_L/D_T = 3$	Iso. $D_L = D_T$	Forch. $D_L = D_T = 0$	Exper.
50	1.21	1.21	1.23	1.23	—
250	3.32	3.38	3.90	3.21	—
494	4.30	4.44	5.46	—	1.5
532	4.41	4.56	5.66	—	1.8
618	4.64	4.81	6.07	—	2.0
712	4.85	5.06	6.48	—	2.3

saturated beds of lead spheres. This experiment was also performed by Jonsson and Catton [26]. These data are included because other low Prandtl number ($Pr_m = 0.018$) experiments are extremely scarce. It is useful to note that, if the analogy with the pure fluid Rayleigh–Bénard problem holds, it is possible that these data points correspond to another convection regime (e.g. unsteady) in which case comparison with our computations is meaningless, cf. Georgiadis [30].

As Table 7 and Fig. 4(f) show, all of the theoretical models used grossly overpredict the heat transfer. In fact, the data extrapolate to a primary bifurcation at a value unrealistically higher than $Ra_m^{crit} = 4\pi^2$. This anomaly warrants further experimental investigation. However, because of the toxic nature of the saturating fluid, further experiments involving mercury are unlikely. A possible alternative is liquid helium.

3.2. *Effect of dispersion*

As shown in Fig. 4, the value of the dispersion coefficients D_L and D_T has significant impact on the heat transfer. The definitions of these two coefficients are given by equations (6b) and (7b). All numerical results reported to this point employ the value $C_L = 0.36$ suggested by Georgiadis and Catton [7]. In the present work, we define $C_T = C_L/4$ for the DFA4 model, and $C_T = C_L/3$ for the DFA3 model. Note that for the DF model, $C_L = C_T = 0$, and for the DFI model $D_T = D_L$. But for the DFA3 and DFA4 models, we have $D_T < D_L$. From the above and equation (5), we conclude that the net heat transfer of the DFA model will be generally less than that of the DFI model (provided (6a) is used for both cases). In fact, the DFI model is an approximate upper bound for the DFA model. This point is made graphically in Fig. 4 and 5. Figure 5 shows temperature surfaces in y–z space (case 1, $\alpha = \pi$, $Ra_m = 200$) for the DFA4 model (solid lines) and the DFI model (dashed lines). Also shown in Fig. 5 are the isotherms for both models, projected onto the plane $(z,y/\lambda)$. The slope of the DFI surface at the $z = 0$ and $z = 1$ boundaries is greater, on average, than the slope of the DFA4 model. According to equation (5), the DFI model will have a higher Nusselt number than the DFA4 model since the temperature gradient is higher. This is confirmed in Fig. 4(a).

One final point concerning dispersion deserves to be made. Hsu and Cheng [10] proposed an expression for transverse dispersion valid at high Reynolds numbers. When compared to equation (7a), their expression is equivalent to ours if we take $C_T = 0.18/4$ and $C_L = 0.18$ for the DFA4 model. Fig. 6 shows a comparison of heat transfer between the DFA4 model using $C_L = 0.36$ and $C_L = 0.18$. It is clear from Fig. 6 that $C_L = 0.18$ gives a better fit to experimental data than $C_L = 0.36$ using the DFA4 model.

3.3. *Rayleigh number–wavenumber space*

Recent experiments in HRLC reveal a variety of stable convective wavepatterns near onset, cf. Howle *et al.* [11]. These experiments, which constitute the first (to our knowledge) direct shadowgraphic visualization of convection in large aspect ratio porous enclosures, indicate that 2-D rolls are the exception rather than the rule in HRLC. It is worth mentioning that, in analogy to the RBC problem, 2-D rolls appear in thin slab-like porous boxes since they are stabilized at the boundaries, as the recent experimental investigation of Lein and Tankin [31] showed. Regarding the laterally unbounded layer, we have to also note that no experiment has contradicted the theoretical prediction of Straus', as revised by Kvernvold and Tyvand [5], that *once 2-D rolls appear* they are stable to infinitesimal disturbances inside a balloon with an apex (at Ra_m^{crit}, $\alpha = \pi$).

All of the heat transfer results reported in the previous section assume $\alpha = \pi$ while Ra_m is changed. Rather than present Nu–α curves with Ra_m held constant, it is more instructive to show the Nu surface in Ra_m–α space, as in Figure 7. This simulation is conducted for case 1 using the DFA4 model with $C_L = 0.36$. Note that the wave number in Fig. 7 has been normalized with π. In the course of numerical simulation we observe that the numerical scheme converges for large wavenumbers all the way to the conduction regime delineated by the neutral curve. For small wavenumbers, another phenomenon is observed for the anisotropic dispersive scheme. Depending on the Ra_m number, there are wavenumbers which lead to a 'numerical bifurcation'. This is manifested by an increase in the number of original rolls as the numerical iterations proceed. Although these solutions need further careful investigation, their appearance might imply that the two-dimensional steady convection regime becomes unstable. We would like to mention

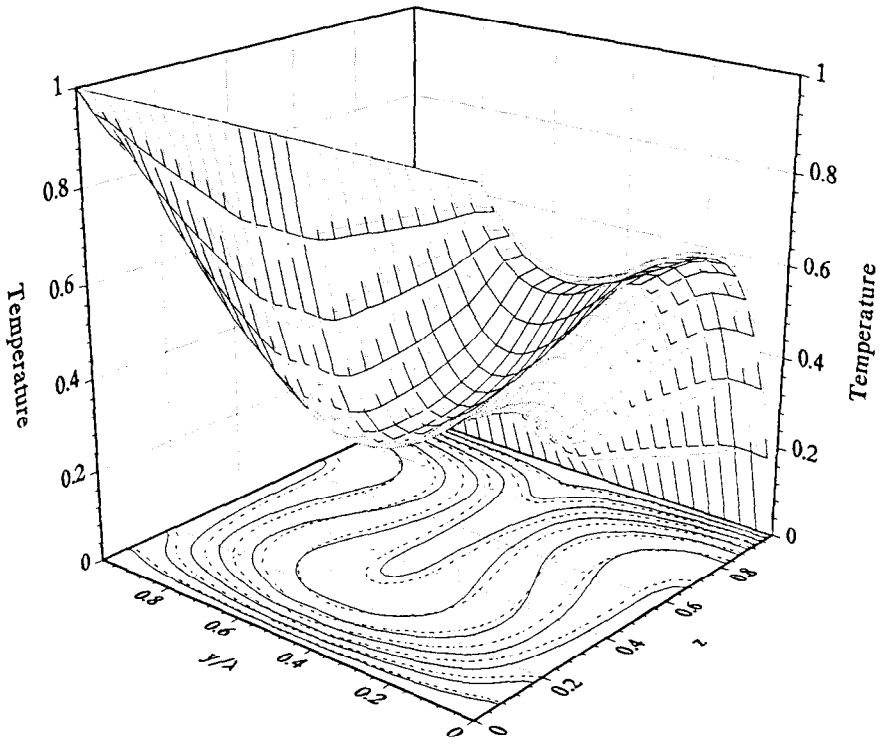

FIG. 5. Temperature surfaces and contours in y–z space for the DFA4 model (solid lines) and the DFI model (dashed lines). Case 1, $\alpha = \pi$, $Ra_m = 200$.

in passing that this domain above the neutral curve is occupied by the sinusoidal instability regime (which is a three-dimensional convection regime), according to Joseph's [3] Darcy model.

Lister [28] found the wavenumber of three-dimensional convection cells to be a function of Rayleigh number. It should be noted that the observation of three-dimensional cells is not consistent with our model consisting of two-dimensional rolls, as depicted in Fig. 1. However, lacking better data, we adapt the measured curve to the two-dimensional case. Lister gives the equation

$$n = 17 + 0.024\, Ra_m \tag{38}$$

for the number of hexagonal convection cells. We will use his slope but change the intercept. The new equation,

$$n = 24.05 + 0.024\, Ra_m \tag{39}$$

gives a hexagonal cell which is two layer depths across the flats ($\alpha^{crit} = \pi$) when $Ra_m^{crit} = 4\pi^2$. The area, A, of the convection cell in terms of the area, A_L, of Listers' experimental apparatus is

$$A = \frac{A_L}{n} = \frac{A_L}{24.05 + 0.024\, Ra_m} \tag{40}$$

where we use (39) rather than (38) for the number of cells. Next, the width of a hexagon (distance across the flats)

$$W = 1.0746\sqrt{A} \tag{41}$$

is scaled with the height, L, to give

$$\lambda = \frac{W}{L}. \tag{42}$$

Then, the area of Listers' experimental apparatus is substituted into (40), the result substituted into (41), and this substituted into (42) to yield, after some manipulation, the wavelength as a function of Ra_m:

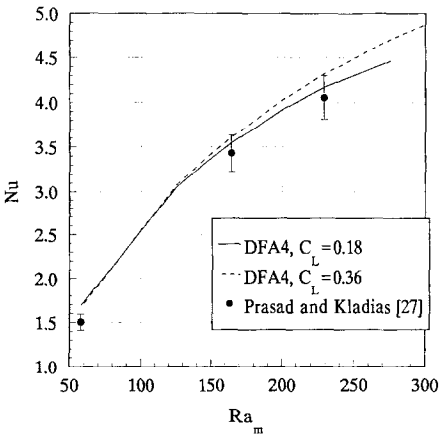

FIG. 6. Comparison of heat transfer using the values $C_L = 0.18$ from Hsu and Cheng [10] and $C_L = 0.36$ from Georgiadis and Catton [7]. Case 1, $\alpha = \pi$, DFA4 model.

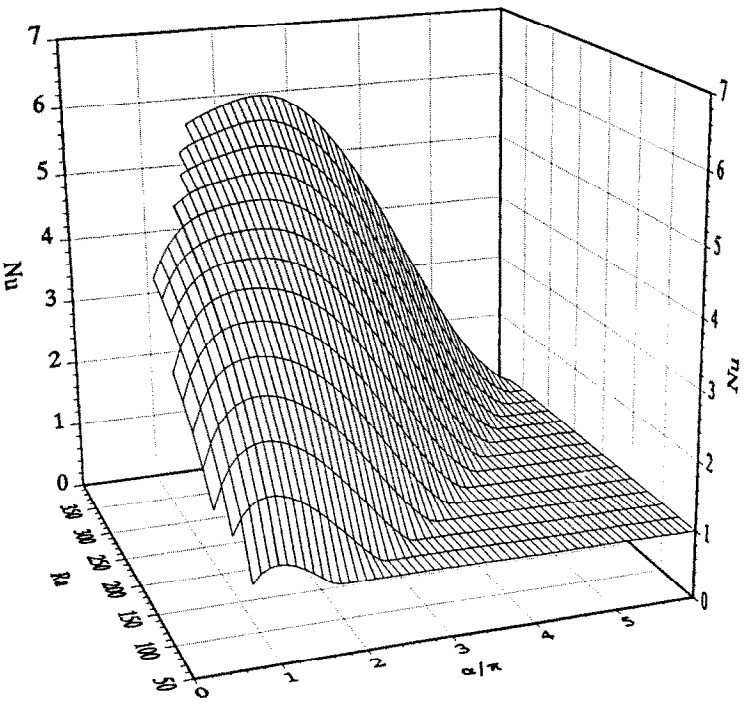

FIG. 7. The Nusselt number surface in Ra_m–α space. Case 1, DFA4 model, $C_L = 0.36$. The thick line corresponds to $\alpha/\pi = 1$.

$$\lambda(Ra_m) = (24 \times 10^{-2} + 24 \times 10^{-5} Ra_m)^{1/2}. \quad (43)$$

Finally, we have the wavenumber as a function of Ra_m:

$$\alpha(Ra_m) = 2\pi(24 \times 10^{-2} + 24 \times 10^{-5} Ra_m)^{1/2}. \quad (44)$$

Figure 8 compares the Nusselt number obtained by using equation (44) with the Nusselt number by using $\alpha = \pi$. In both computations, the DFA4 model with $C_L = 0.36$ is used. Although the wavenumber varies by 10% over the range of the Rayleigh number studied, the effect on Nusselt number is small. We note in closing that Lein and Tankin [31] reported that the wavenumber did not vary with Ra_m in slab-like porous boxes.

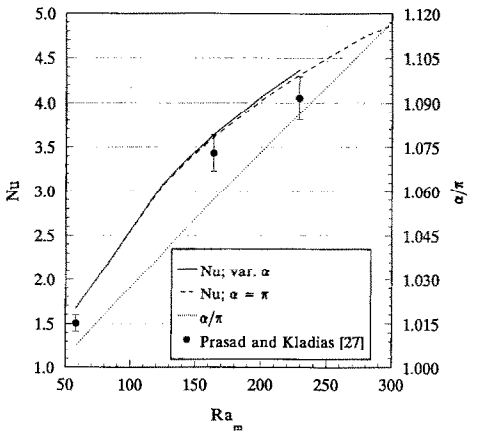

FIG. 8. Comparison between heat transfer using $\alpha = \pi$ and equation (44). Case 1, DFA4 model, $C_L = 0.36$.

4. CONCLUSIONS AND FUTURE NEEDS

A parametric numerical exploration of steady, two-dimensional cellular convection in packed beds using a dispersive non-Darcy model with anisotropic conductivity revealed the following.

1. The inclusion of a hydrodynamic dispersion term brings an increase of the net heat transfer rate, as expressed by the Nusselt number, after a Rayleigh number value in the range 100–200. After this range, the Nusselt numbers corresponding to the anisotropic dispersive model lie between the isotropic values and those of the pure Forchheimer model (absence of dispersion). As the degree of anisotropy of the effective thermal conductivity is increased, the wall-averaged Nusselt number is decreased. This is consistent with the fact that this Nusselt number depends on the transverse dispersion component since the wall is isothermal and the normal velocity is zero, see equation (5).

2. With the exception of oil–glass systems, all models tend to overpredict the Nu–Ra_m data found in the literature. Better agreement is obtained as the magnitude of the longitudinal dispersion coefficient is decreased from $C_L = 0.36$ to 0.18, as suggested by Hsu and Cheng [10]. The worst cases are water-saturated steel spheres and mercury-saturated lead packed beds. For the water–steel system, this is probably caused by the large variation in the stagnant thermal conductivity estimates in such systems (where the conductivity difference between the two phases is large).

3. In general, the Nusselt number depends strongly

on the wavenumber. Unfortunately available wavenumber measurements are sparse and do not pertain to two-dimensional convection. Our best estimates of wavenumber variation with Ra_m, obtained from the experimental results of Lister [28], do not alleviate the divergence between simulation and experiment.

4. The large scale divergence of the experimental Nu–Ra_m results, as exemplified by Fig. 3, is greatly reduced when we plot Nu vs Ra_m/Ra_m^{crit}. This rescaling effectively eliminates all the thermophysical properties of the particular system except for the stagnant effective thermal conductivity used in the definition of Nu. It is obvious that attention has to be paid to determining these coefficients, such as the thermal conductivity from direct experiments. Existing references of experimental investigation do not report error bars of the thermophysical and structural parameters used to reduce the data. At the same time, a more systematic investigation of the porous Rayleigh–Bénard problems needs to be undertaken. Finally, progress in the area of pattern visualization of convection in packed beds is needed before further simulation is attempted. We will report in the future on progress towards this goal.

Acknowledgements—We are grateful for the financial support of the National Science Foundation under grants CTS-8909119 and CTS-9006189 and the U.S. Department of Energy (Office of Basic Energy Sciences) under grant DE-FG05-90ER14141. We would also like to thank Professor Robert Behringer of Duke University and Professor David Poirier of University of Arizona for their helpful suggestions.

REFERENCES

1. J. G. Georgiadis, Future research needs in heat and mass transport in porous media. In *Convective Heat and Mass Transfer in Porous Media* (Edited by S. Kakac *et al.*), NATO ASI Series E, Vol. **196,** pp. 1073–1088. Kluwer, Norwell (1991).
2. D. A. Nield and A. Bejan, *Convection in Porous Media*. Springer, New York (1991).
3. D. D. Joseph, *Stability of Fluid Motions II*. Springer, Berlin (1976).
4. H. Neischloss and G. Dagan, Convective currents in a porous layer heated from below: the influence of hydrodynamic dispersion, *Phys. Fluids* **18,** 757–761 (1975).
5. O. Kvernvold and P. Tyvand, Dispersion effects on thermal convection in porous media, *J. Fluid Mech.* **99,** 673–686 (1980).
6. J. G. Georgiadis and I. Catton, An effective equation governing convective transport in porous media, *J. Heat Transfer* **110,** 635–641 (1988).
7. J. G. Georgiadis and I. Catton, Dispersion in cellular thermal convection in porous layers, *Int. J. Heat Mass Transfer* **31,** 1081–1091 (1988).
8. X. S. He and J. G. Georgiadis, Direct numerical simulation of diffusion problems with intrinsic randomness, *Int. J. Heat Mass Transfer* **35,** 3141–3151 (1992).
9. P. G. Saffman, Dispersion due to molecular diffusion and macroscopic mixing in fluid through a network of capillaries, *J. Fluid Mech.* **7,** 194–208 (1960).
10. C. Hsu and P. Cheng, Thermal dispersion in a porous medium, *Int J. Heat Mass Transfer* **33,** 1587–1597 (1990).
11. L. E. Howle, R. P. Behringer and J. G. Georgiadis, Visualization of convective fluid flow in a porous medium, *Nature* **362,** 230–232 (1993).
12. S. Ergun, Fluid flow through packed columns, *Chem. Engng Prog.* **48,** 89–94 (1952).
13. G. I. Taylor, Dispersion of soluble matter in solvent flowing slowly through a tube, *Proc. Roy. Soc.* **A219,** 186–203 (1953).
14. J. Levec and R. Carbonell, Longitudinal and lateral thermal dispersion in packed beds, Parts I & II, *A.I.Ch.E. J.* **31,** 581–602 (1985).
15. L. E. Howle, Simulation of natural convection in porous media: anisotropic dispersive thermal conductivity, Master of Science Thesis, Duke University (1991).
16. R. A. Wooding, An experiment on free thermal convection of water in saturated permeable material, *J. Fluid Mech.* **3,** 582–600 (1958).
17. K. J. Schneider, Investigation of the influence of free thermal convection on heat transport through granular material, *Proc. 11th Int. Cong. of Refrigeration*, Paper II-4, pp. 247–254. Pergamon Press, Oxford (1963).
18. J. W. Elder, Steady free convection in a porous medium heated from below, *J. Fluid Mech.* **27,** 29–48 (1967).
19. Y. Katto and T. Masuoka, Criterion for the onset of convective flow in a fluid in a porous medium, *Int. J. Heat Mass Transfer* **10,** 297–309 (1967).
20. M. Combarnous, Convection naturelle et convection mixte dans une couche poreuse horizontale, *Rev. Gén. Thermique* **9,** 1355–1375 (1970).
21. T. Kaneko, M. Mohtadi and K. Aziz, An experimental study of natural convection in inclined porous media, *Int. J. Heat Mass Transfer* **17,** 485–496 (1974).
22. Y. C. Yen, Effects of density inversion on free convective heat transfer in porous layer heated from below, *Int. J. Heat Mass Transfer* **17,** 1349–1356 (1974).
23. M. A. Combarnous and S. A. Bories, Hydrothermal convection in saturated porous media, *Adv. Hydrosci.* **10,** 231–307 (1975).
24. R. J. Buretta and A. S. Berman, Convective heat transfer in a liquid saturated porous layer, *ASME J. Appl. Mech.* **43,** 249–253 (1976).
25. V. Prasad, F. A. Kulacki and M. Keyhani, Natural convection in porous media, *J. Fluid Mech.* **150,** 89–119 (1985).
26. T. Jonsson and I. Catton, Prandtl number dependence of natural convection in porous media, *ASME J. Heat Transfer* **109,** 371–377 (1987).
27. V. Prasad and N. Kladias, Non-Darcy natural convection in saturated porous media. In *Convective Heat and Mass Transfer in Porous Media* (Edited by S. Kakac *et al.*), NATO ASI Series E, Vol. **196,** pp. 173–224. Kluwer, Norwell (1991).
28. C. R. B. Lister, An explanation for the multivalued heat transport found experimentally for convection in a porous medium, *J. Fluid Mech.* **214,** 287–320 (1990).
29. J. L. Lage, A. Bejan and J. G. Georgiadis, The Prandtl number effect near the onset of Bénard convection in a porous medium, *Int. J. Heat Fluid Flow* **13,** 408–411 (1992).
30. J. G. Georgiadis, Was Lord Rayleigh right?, *ASME J. Heat Transfer* **13,** 408–411 (1992).
31. H. Lien and R. S. Tankin, Natural convection in porous media—I. Nonfreezing, *Int. J. Heat Mass Transfer* **35,** 175–186 (1992).